Electronic Supplementary Material (ESI) for Dalton Transactions.

[Supporting Information]

# $CO_2$ Adsorption-Induced Structural Changes in Coordination Polymer Ligands Elucidated via Molecular Simulations and Experiments

Paul J. Meza-Morales,[a] Diego A. Gómez-Gualdrón,[b] Rodinson A. Arrieta-Perez,[a] Arturo J. Hernandez-Maldonado,[a] Randall Q. Snurr,[b] and María C. Curet-Arana[a*]

[a] Department of Chemical Engineering, University of Puerto Rico - Mayaguez Campus, Road 108 - km 1.1, Mayaguez, PR 00681-9000, United States

[b] Department of Chemical and Biological Engineering, Northwestern University, 2145 Sheridan Road, Evanston, IL 60208, United States

*Corresponding Author: Department of Chemical Engineering, University of Puerto Rico - Mayaguez Campus, Call Box 9000, Mayaguez, PR 00681-9000, United States, Fax:787 265-3818, Tel.: 787 832-4040 ext. 2569, E-mail: maria.curetarana@upr.edu

**Table of Contents**

## Section S1. Unit cell and unit cell deformation for CPL-2

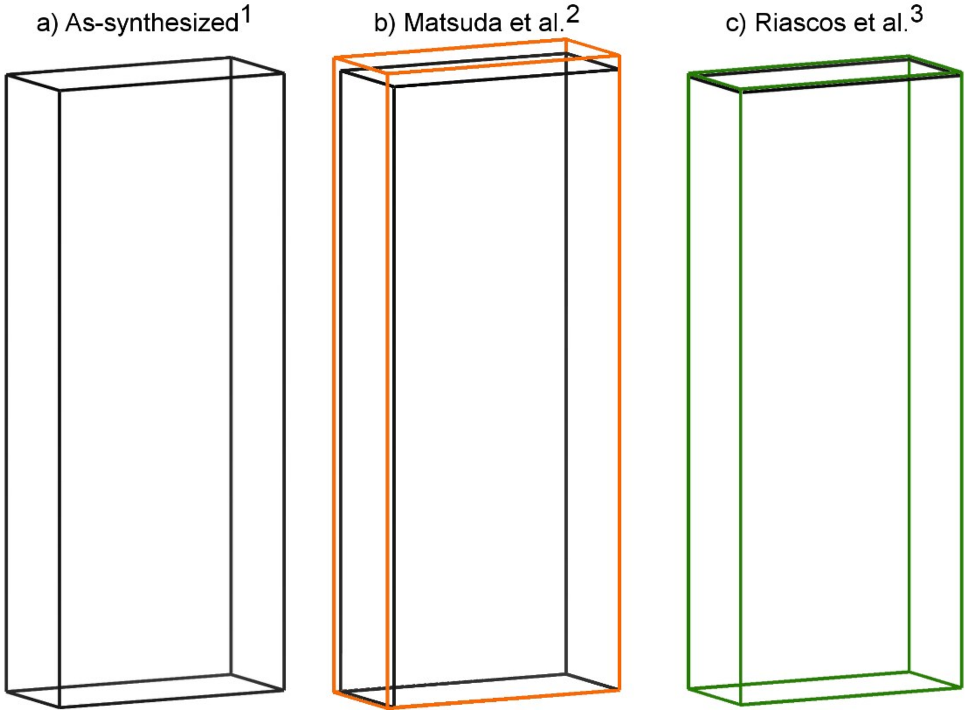

**Fig. S1** Comparison between the unit cell of the as-synthesized CPL-2[1] with the unit cell deformation reported by Kitagawa and co-workers[2] and Hernandez-Maldonado and co-workers.[3] (a) unit cell of as-synthesized CPL-2 (black box), (b) unit cell of CPL-2 based on the deformation reported by Kitagawa and co-workers[2] (orange box), and (c) unit cell of CPL-2 based on the deformation reported by Hernandez-Maldonado and co-workers[3] (green box).

## Section S2: Force field parameters

**Table S1.** LJ parameters from the UFF force field

| Atom | $\varepsilon/k_B$ [K] | $\sigma$ [Å] |
|---|---|---|
| Cu | 2.516 | 3.114 |
| O | 30.192 | 3.119 |
| N | 34.721 | 3.261 |
| C | 52.836 | 3.431 |
| H | 22.141 | 2.572 |

**Table S2.** TraPPE parameters for $CO_2$

| Atom | Type | $\varepsilon/k_B$ [K] | $\sigma$ [Å] | q [e] |
|---|---|---|---|---|
| C | O=[C]=O | 27.0 | 2.80 | 0.7 |
| O | [O]=C=O | 79.0 | 3.05 | -0.35 |
| O | O=C=[O] | 79.0 | 3.05 | -0.35 |

**Table S3.** TraPPE parameters for $N_2$

| Atom | Type | $\varepsilon/k_B$ [K] | $\sigma$ [Å] | q [e] |
|---|---|---|---|---|
| N | [N]=Ncom=N | 36 | 3.31 | -0.482 |
| Ncom | N=[Ncom]=N | 0 | 0 | 0.964 |
| N | N=Ncom=[N] | 36 | 3.31 | -0.482 |

## Section S3: Atomic charges

Fig. S2 to S4 show the simplified cluster models (CPL-representative cluster model), which correspond to a corner of the CPL pore channel, used to estimate framework charges. The obtained charges were assigned to the atoms in the asymmetric unit cell ensuring a total zero charge on the framework.

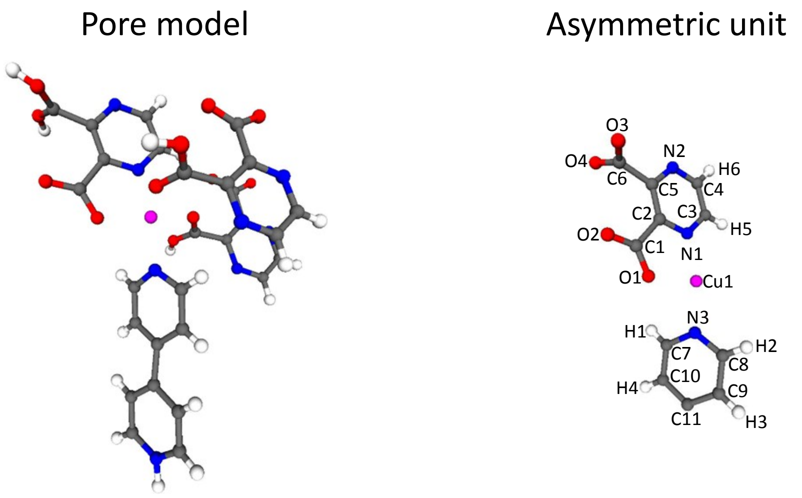

| Atom_site_label | Atom_site_charge |
|---|---|
| Cu1 | 0.577 |
| O1 | -0.763 |
| O2 | -0.694 |
| O3 | -0.571 |
| O4 | -0.623 |
| N1 | 0.153 |
| N2 | -0.763 |
| N3 | -0.074 |
| C1 | 0.931 |
| C2 | -0.375 |
| C3 | -0.193 |
| C4 | 0.604 |
| C5 | 0.490 |
| C6 | 0.820 |
| C7 | 0.106 |
| C8 | 0.033 |
| C9 | -0.269 |
| C10 | -0.259 |
| C11 | 0.100 |
| H1 | 0.116 |
| H2 | 0.087 |
| H3 | 0.198 |
| H4 | 0.126 |
| H5 | 0.239 |
| H6 | 0.004 |

**Fig. S2** Pore model, asymmetric unit cell, and atomic charges for CPL-2

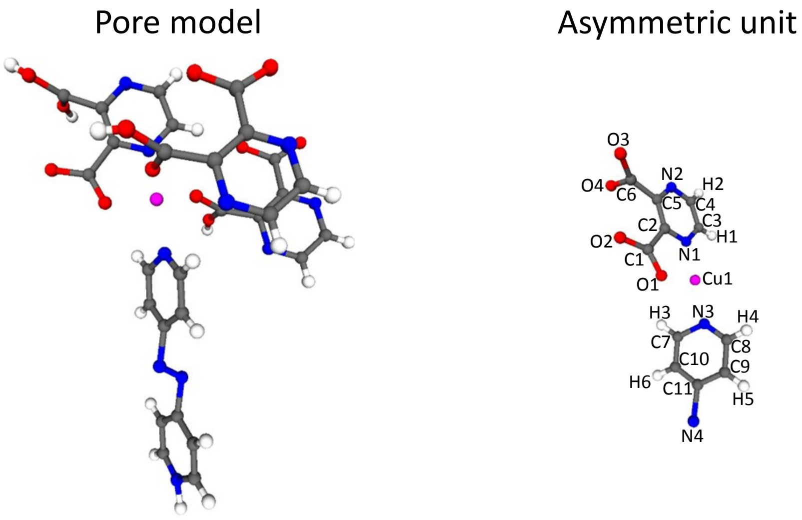

Pore model

Asymmetric unit

| Atom_site_label | Atom_site_charge |
|---|---|
| Cu1 | 0.690 |
| O1 | -0.666 |
| O2 | -0.645 |
| O3 | -0.891 |
| O4 | -0.629 |
| N1 | 0.532 |
| N2 | -0.772 |
| N3 | -0.145 |
| N4 | -0.426 |
| C1 | 0.692 |
| C2 | -0.239 |
| C3 | -0.232 |
| C4 | 0.644 |
| C5 | 0.423 |
| C6 | 0.877 |
| C7 | 0.207 |
| C8 | 0.257 |
| C9 | -0.556 |
| C10 | -0.537 |
| C11 | 0.693 |
| H1 | 0.254 |
| H2 | -0.045 |
| H3 | 0.029 |
| H4 | -0.032 |
| H5 | 0.270 |
| H6 | 0.247 |

**Fig. S3** Pore model, asymmetric unit cell, and atomic charges for CPL-4

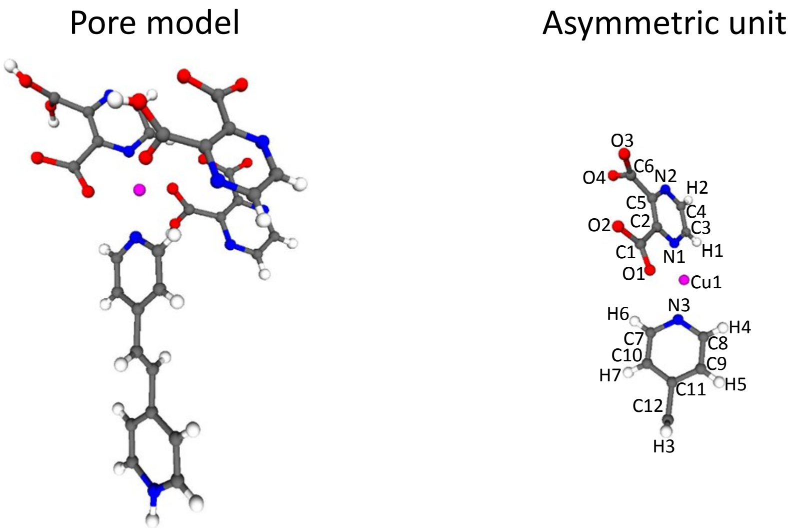

Pore model

Asymmetric unit

| Atom_site_label | Atom_site_charge |
|---|---|
| Cu1 | 0.731 |
| O1 | -0.613 |
| O2 | -0.651 |
| O3 | -0.789 |
| O4 | -0.465 |
| N1 | -0.044 |
| N2 | -0.683 |
| N3 | -0.288 |
| C1 | 0.609 |
| C2 | -0.106 |
| C3 | -0.116 |
| C4 | 0.539 |
| C5 | 0.338 |
| C6 | 0.834 |
| C7 | 0.247 |
| C8 | 0.289 |
| C9 | -0.423 |
| C10 | -0.358 |
| C11 | 0.360 |
| C12 | 0.092 |
| H1 | 0.242 |
| H2 | 0.002 |
| H3 | 0.021 |
| H4 | 0.001 |
| H5 | 0.198 |
| H6 | 0.073 |
| H7 | 0.144 |

**Fig. S4** Pore model, asymmetric unit cell, and atomic charges for CPL-5

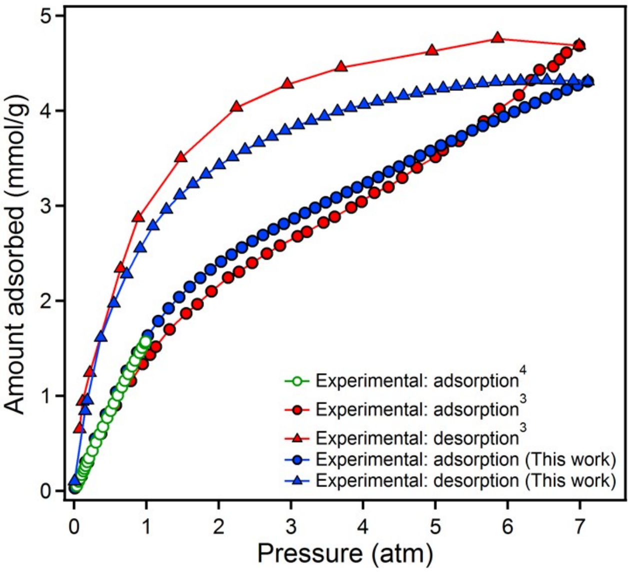

**Fig. S5** Comparison between experimental $CO_2$ adsorption/desorption isotherms at 298 K measured here and reported ones. The reported experimental isotherms were taken from Hernandez-Maldonado and co-workers.[3,4]

## Section S4: Force field validation

To validate our force field, the carbon dioxide isotherms for the metal-organic framework NU-125, which includes the same types of atoms as the CPLs studied here (Cu, N, O, C, and H), were reproduced. Fig. S6 compares our results for $CO_2$ adsorption isotherms on NU-125 with those reported by Wilmer et al.[5] In general, it can be observed that our results are consistently in good agreement with the experimental isotherm previously reported by Wilmer and coworkers.

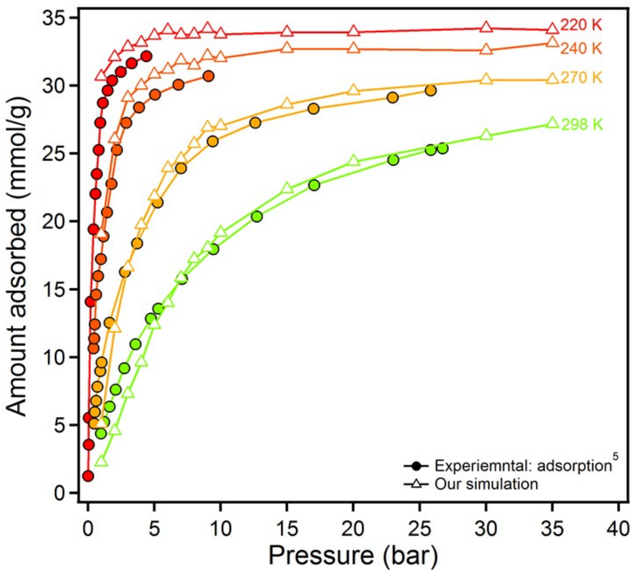

**Fig. S6** Comparison between the simulated and experimental[5] $CO_2$ adsorption isotherms on NU-125, a nanoporous material with similar atoms as CPL-2. The solid lines with filled circles correspond to the experimental results reported by Wilmer et al.[5] The solid lines with empty triangles symbols correspond to our simulation results.

## Section S5: Textural properties for CPL-n-(*a*) structures

**Nitrogen adsorption isotherm.** Fig. S7 compares experimental and simulated nitrogen adsorption isotherms at 77 K for CPL-2-(***a***), CPL-4-(***a***) and CPL-5-(***a***).

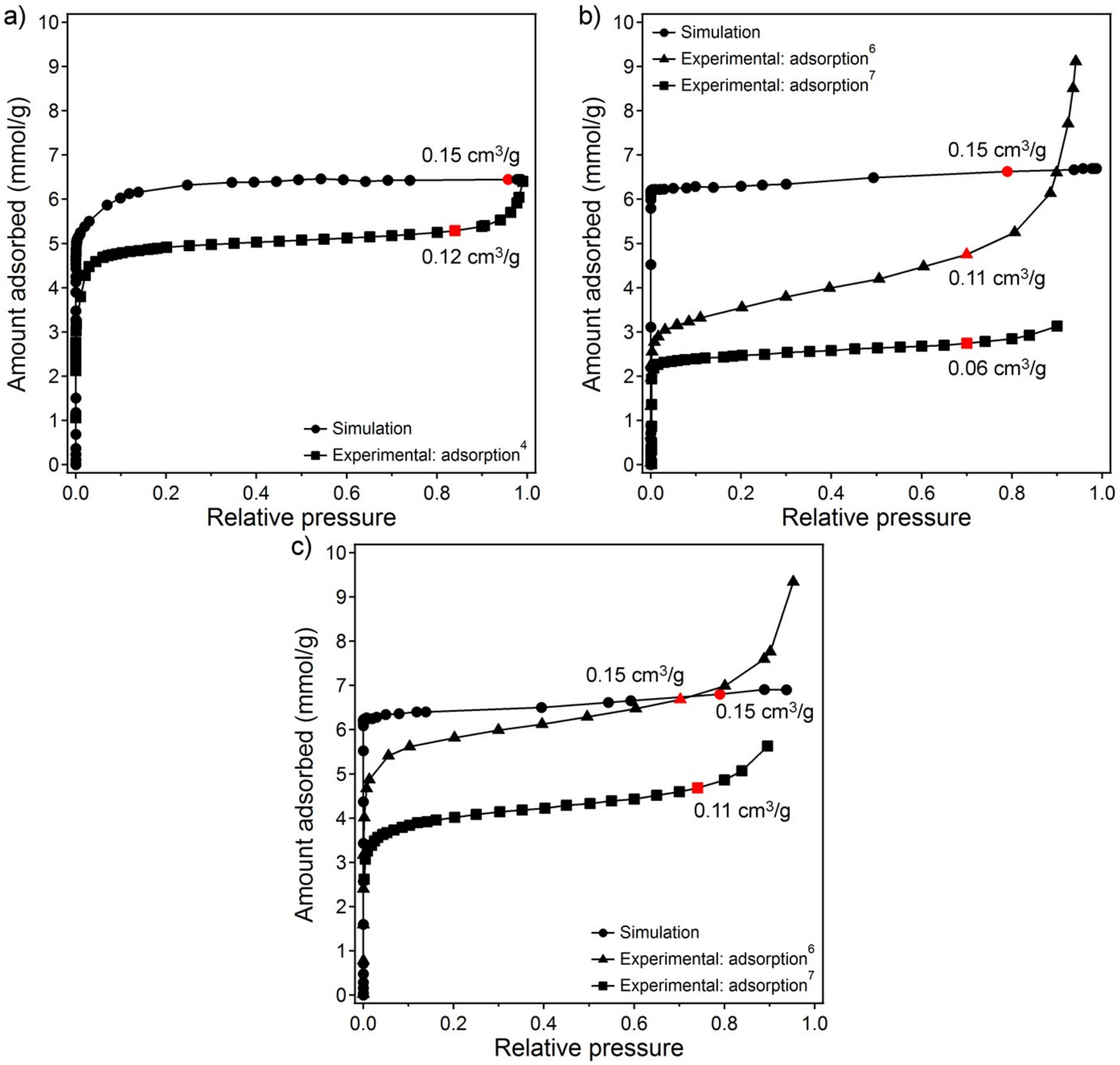

**Fig. S7** Comparison between experimental and simulated (on CPL-n-(***a***)) $N_2$ adsorption isotherms at 77 K on a) CPL-2, b) CPL-4 and c) CPL-5. The experimental isotherms were taken from Kitagawa and co-workers[6] and Hernandez-Maldonado and co-workers.[4,7] The red symbols are adsorption points at saturation loading selected to calculate the pore volumes annotated for each isotherm. For consistency in comparing simulation and experiments, in the main text we report the pore volumes calculated from nitrogen isotherms in ref. 4 and ref. 7, since experimental $CO_2$ isotherms discussed in the main text were also taken from ref. 7 (no $CO_2$ isotherms were reported in ref. 6).

From the saturation loading, pore volumes were calculated as follow:

$$[Amount\ adsorbed]_{saturation\ loading}\frac{mmol\ N_2}{g\ CPL-n}\frac{1\ mol\ N_2}{1000\ mmol\ N_2}\frac{28.02\ g\ N_2}{1\ mol\ N_2}\frac{1\ cm^3\ N_2}{0.81\ g\ N_2}$$

BET areas[8] were calculated using the BET isotherm:

$$\upsilon = \frac{\upsilon_m C\left({}^{P}/_{P_0}\right)}{\left(1 - {}^{P}/_{P_0}\right)\left[1 + (C - 1){}^{P}/_{P_0}\right]}$$

which can be expressed in linearized form:

$$\frac{\left({}^{P}/_{P_0}\right)}{\upsilon\left(1 - {}^{P}/_{P_0}\right)} = \frac{1}{\upsilon_m C} + \frac{(C - 1)}{\upsilon_m C}\left({}^{P}/_{P_0}\right)$$

where $P/P_0$ corresponds to the equilibrium relative pressure, $\upsilon$ is the adsorbed amount at the equilibrium relative pressure $P/P_0$, and $\upsilon_m$ is the adsorbed amount corresponding to the BET monolayer (monolayer capacity). The parameter C is associated with the heat of adsorption. The BET areas were calculated considering the Rouquerol consistency criteria[9] from the simulated and experimental adsorption isotherms, as illustrated in Figs. S8 and S9, respectively. From the BET analysis on the simulated isotherms, only CPL-2-(***a***) strictly fulfills the four Rouquerol consistency criteria; CPL-4-(***a***) and CPL-5-(***a***) just satisfy the first two criteria. On another hand, in BET analysis for the experimental isotherms, CPL-2, CPL-4 and CPL-5 all strictly fulfill the four Rouquerol consistency criteria.

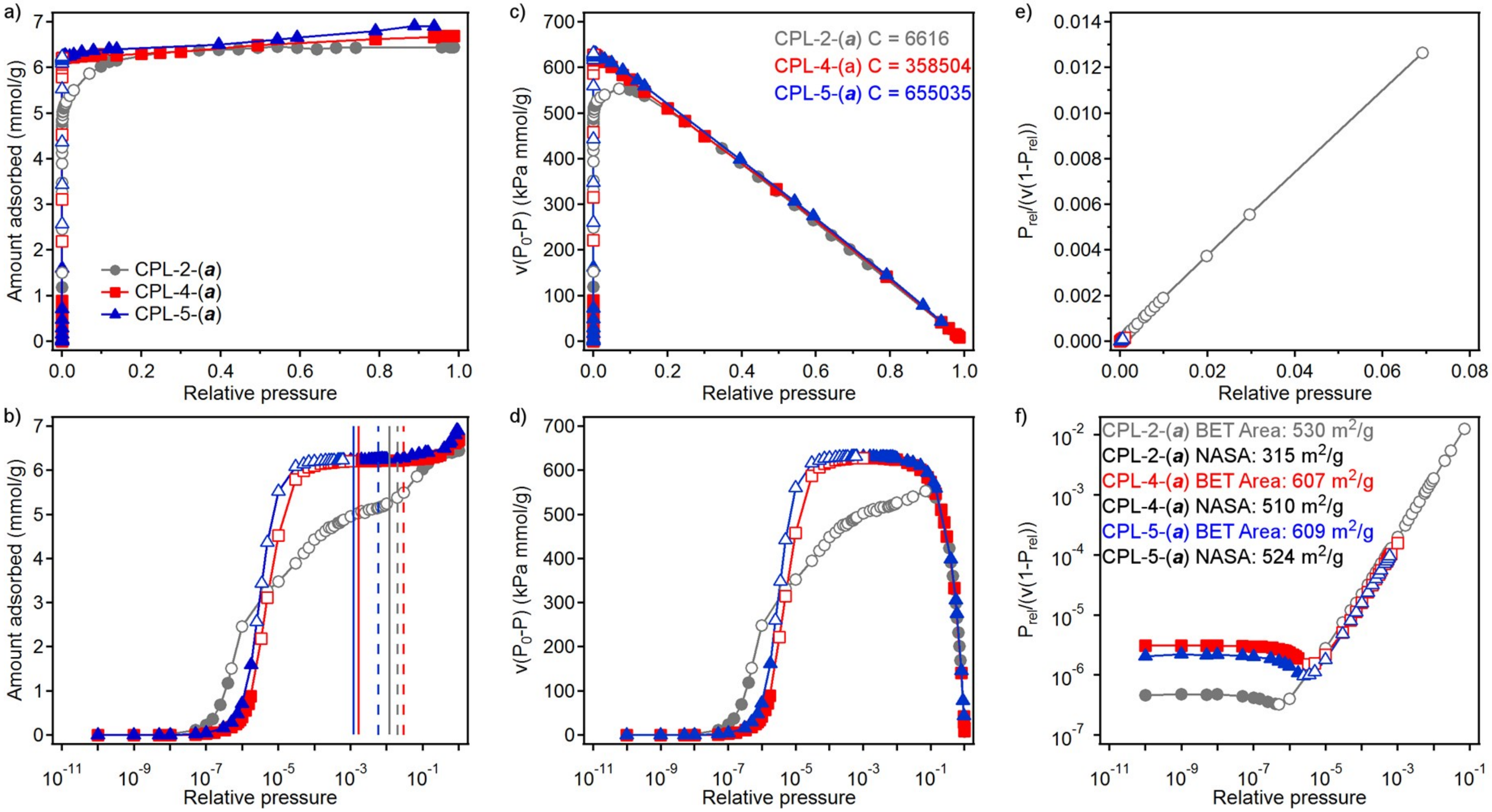

**Fig. S8** BET analysis for CPL-2-(***a***), CPL-4-(***a***) and CPL-5-(***a***) based on simulated isotherms. White markers denote the points used in the BET area calculation. The dash and solid vertical lines indicate the relative pressure values that correspond to the BET-predicted monolayer capacity and calculated by $1/(\sqrt{C} + 1)$, respectively.

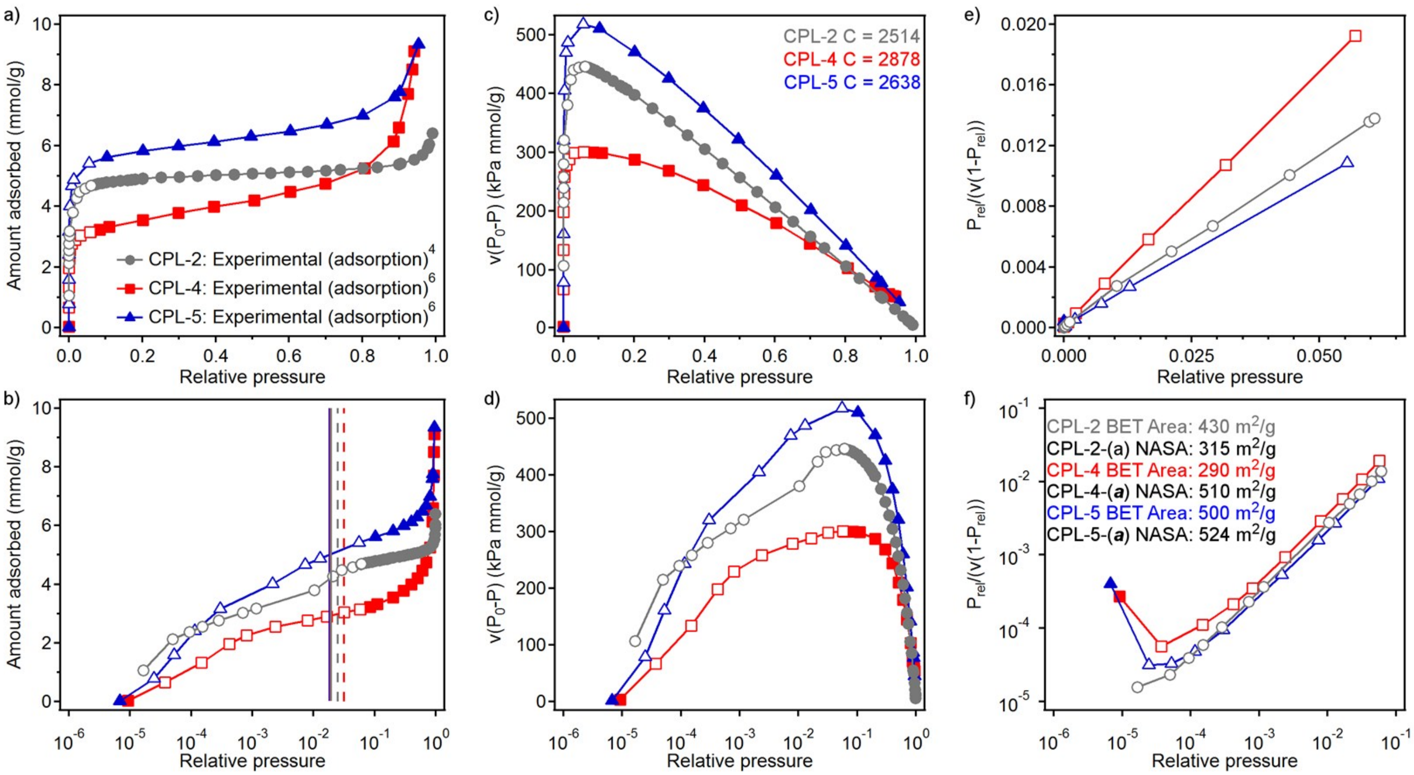

**Fig. S9.** BET analysis for CPL-4 and CPL-5 based on experimental isotherms.[4,6] White markers denote the points used in the BET area calculation. The dash and solid vertical lines indicate the relative pressure values that correspond to the BET-predicted monolayer capacity and calculated by $1/(\sqrt{C} + 1)$, respectively.

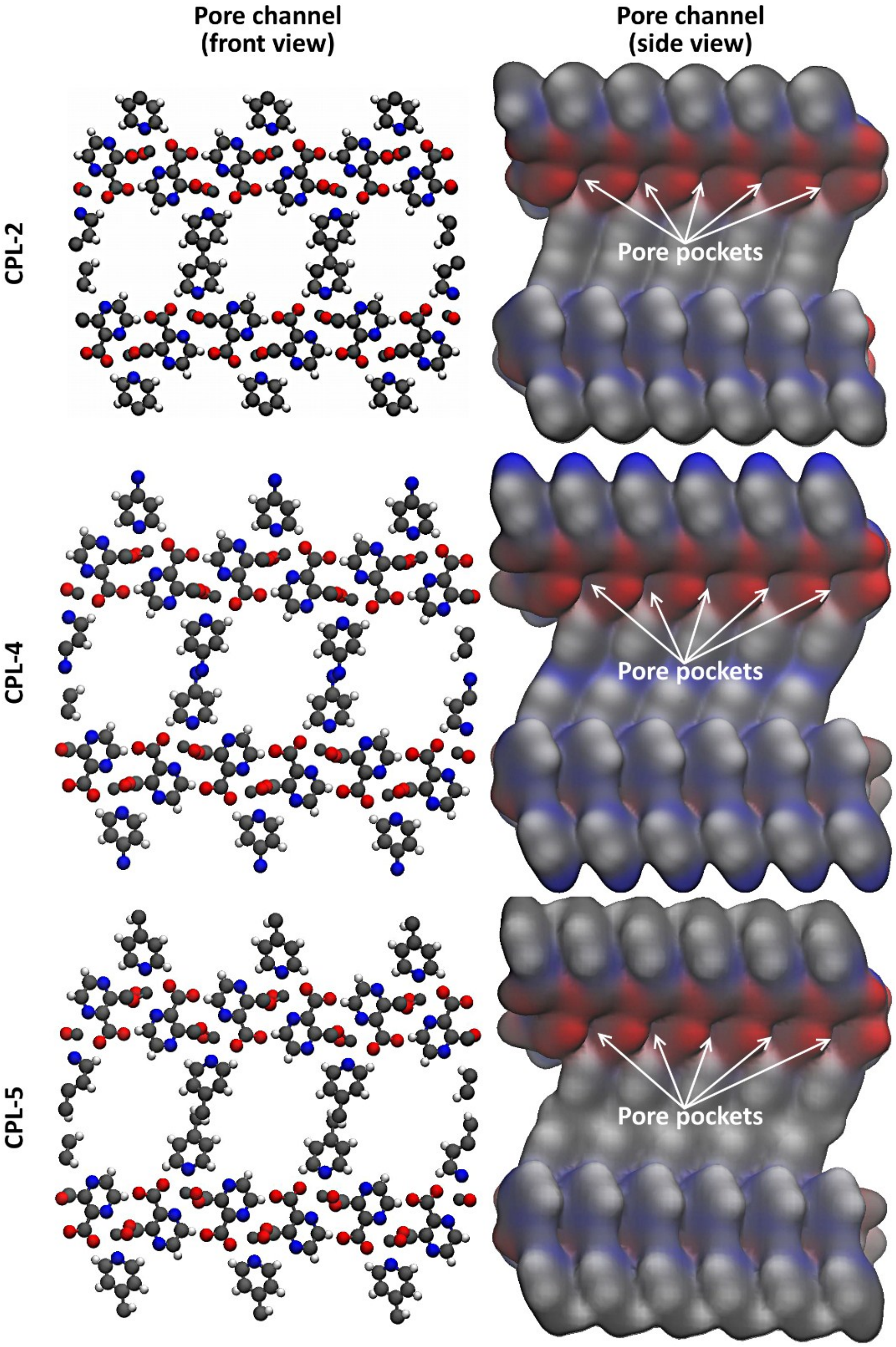

**Fig. S10** Pore channel and pore pockets on CPL-2, CPL-4, and CPL-5.

## Section S6: Adsorption analysis on CPL-2

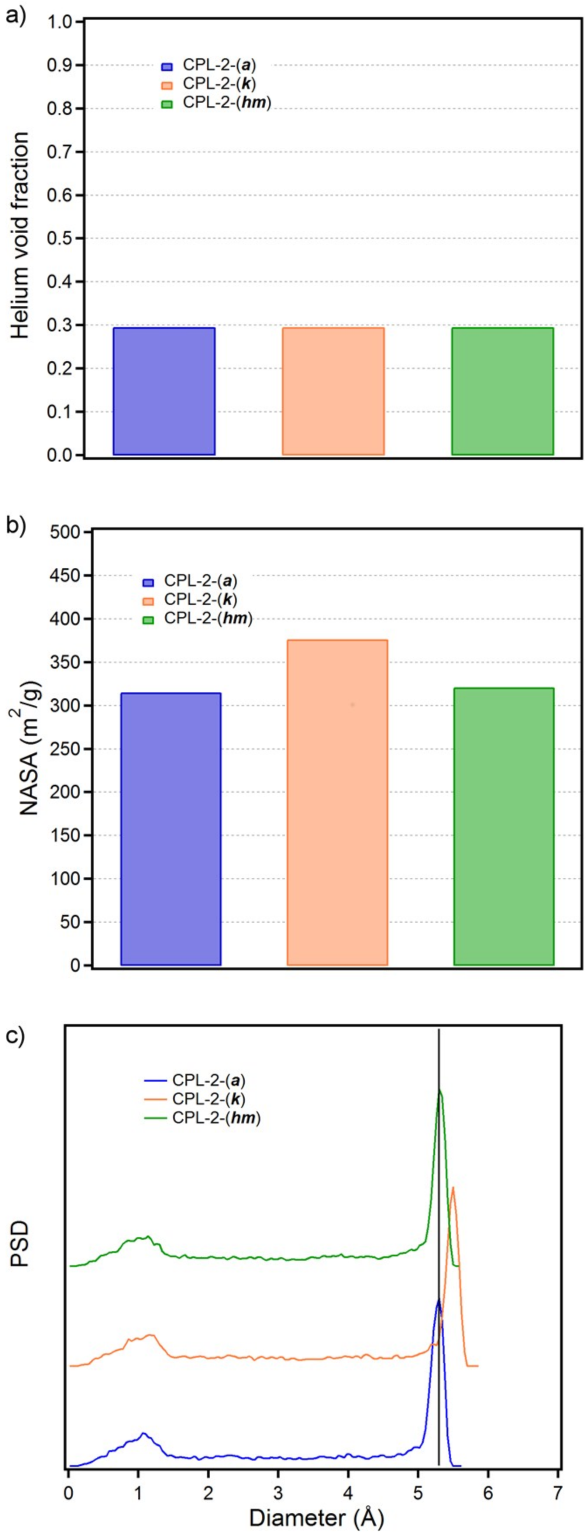

**Fig. S11** Effect of the structural changes reported by Kitagawa and co-workers[2] and Hernandez-Maldonado and co-workers[3] on CPL-2 textural properties: (a) helium void fraction, (b) nitrogen accessible surface area (NASA) and (c) pore size distribution (PSD).

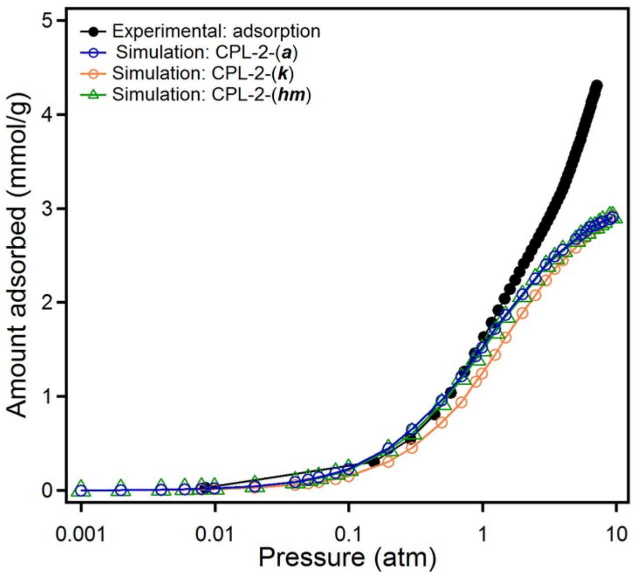

**Fig. S12** Comparison between the simulated and experimental $CO_2$ adsorption isotherm on CPL-2 at 298 K in semi-log scale. Simulated isotherms were obtained with the crystallographic structures of CPL-2-(***a***), CPL-2-(***k***) and CPL-2-(***hm***).

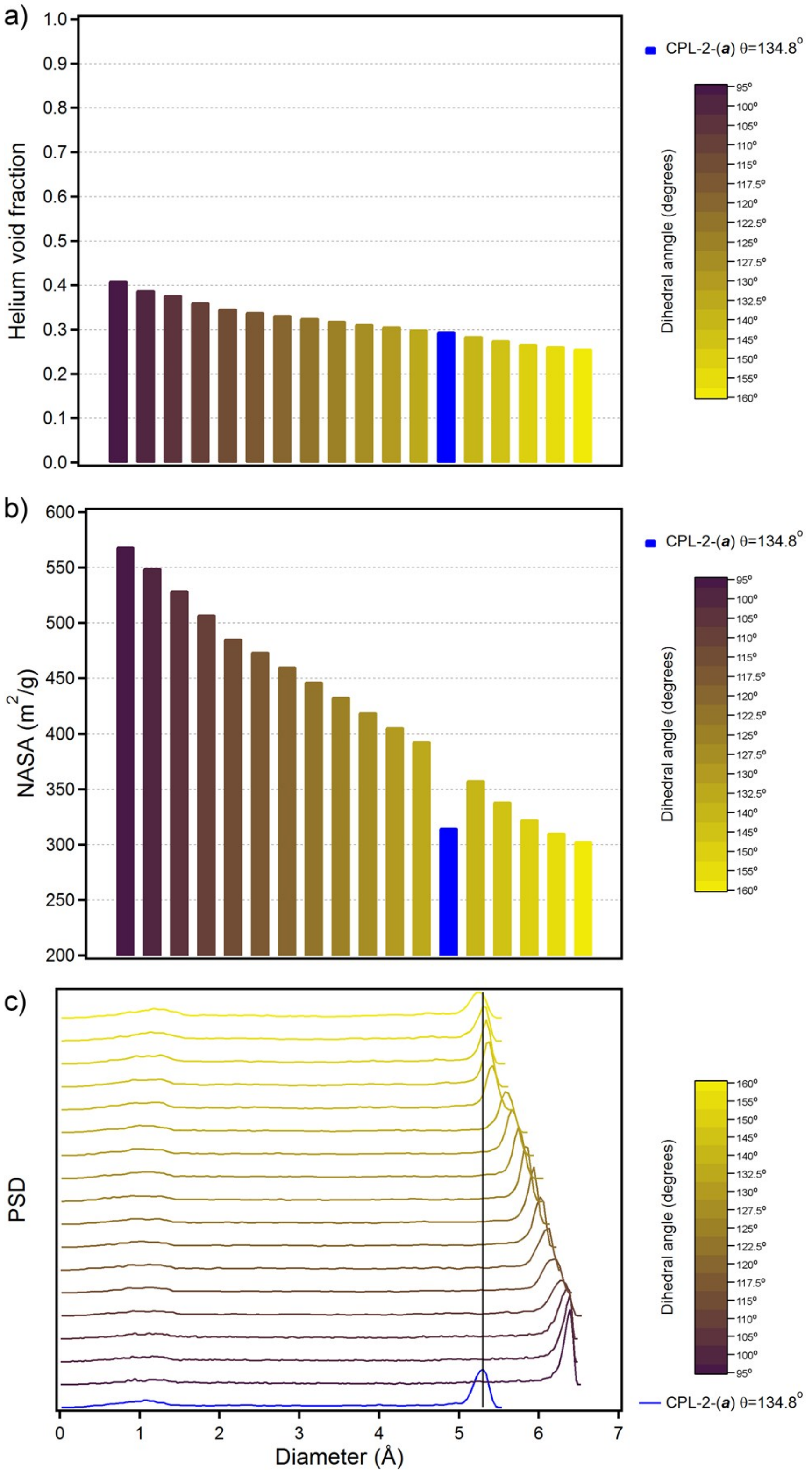

**Fig. S13** Effect of the ligand rotation on CPL-2-(***lr***) (color gradient) textural properties and comparison with CPL-2-(***a***) (blue): (a) helium void fraction, (b) nitrogen accessible surface area (NASA) and (c) pore size distribution. Recall that unit cell parameters of CPL-2-(***a***) and CPL-2-(***lr***) are different, because CPL-2(***lr***) is based on CPL-2-(***k***)

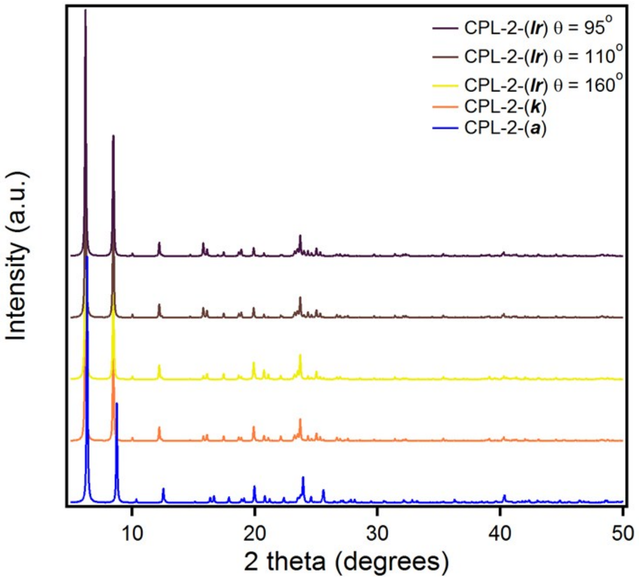

**Fig. S14** Comparison of simulated PXRDs for CPL-2-(***a***), CPL-2-(***k***) and CPL-2-(***lr***) (for different degrees of ligand rotation)

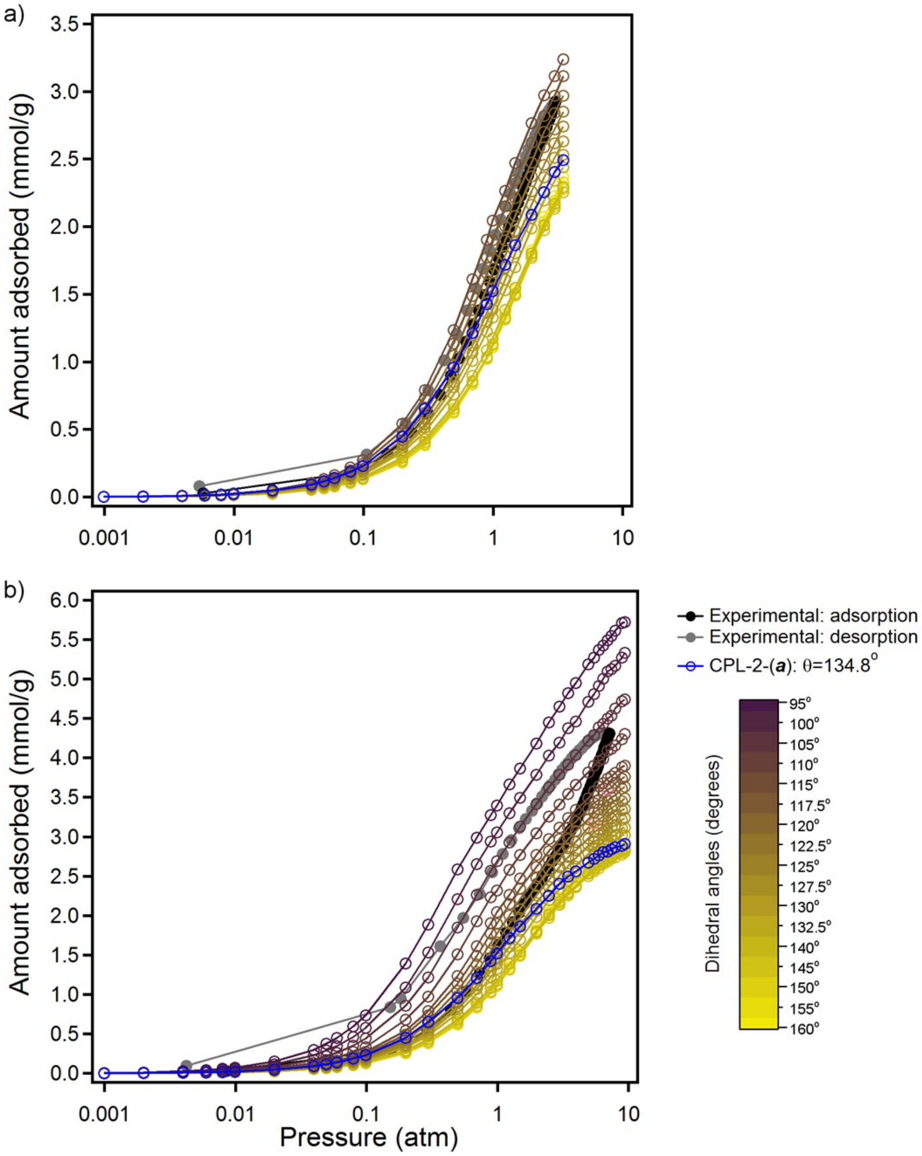

**Fig. S15** Comparison between the simulated (empty circles) and experimental adsorption/desorption (solid circles) $CO_2$ isotherms on CPL-2 at 298 K. The simulated isotherms were calculated on CPL-2-(***lr***) for different angles of *bpy* rotation (color gradient) and for CPL-2-(***a***) (blue).

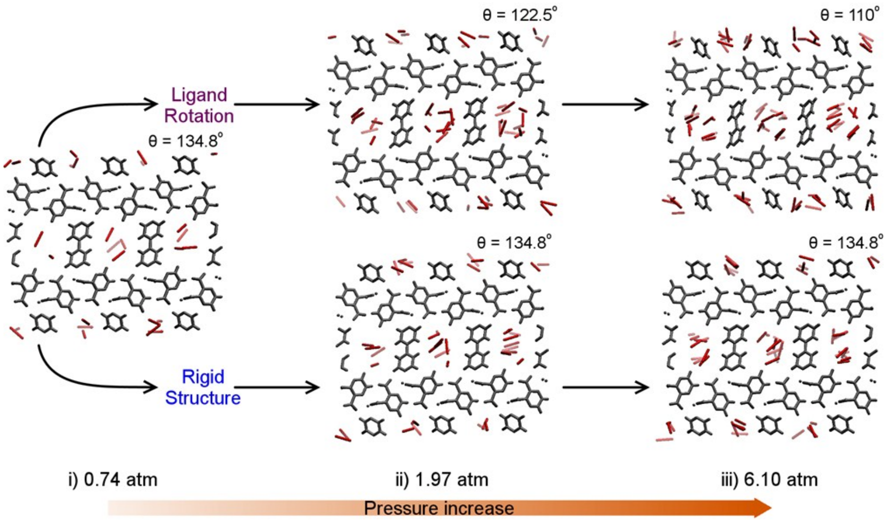

**Fig. S16**. $CO_2$ snapshots on CPL-2-(***a***) (θ = 134.8˚) and CPL-2-(***lr***) structures for *bpy* rotations of θ = 122.5° and 110°. $CO_2$ molecules are shown in red, CPL-2 atoms are shown in gray.

To further look into hysteresis, we performed two-cycle adsorption/desorption experiments on a CPL-2 sample (Fig. S17). Both experiments were performed on the same sample. In each experiment, the adsorption/desorption cycles were gathered up to 3.0 and 7.0 atm, respectively. It can be noted from Fig. S17 that the hysteresis for the adsorption/desorption cycles gathered up to 7.0 atm is much higher than the hysteresis obtained when the cycles were carried out up to 3 atm. These observations are also in agreement with our simulations, which suggest that this difference is a consequence of the structural changes that CPL-2 undergoes. Our simulations indicate that at pressures below 3 atm, unit cell deformations take place with a slight *bpy* ligand rotation. However, as the $CO_2$ loading increases, the CPL-2 framework undergoes structural changes involving a higher degree of *bpy* ligand rotation. In general, in both cases, the second adsorption/desorption cycle is slightly higher than the first one.

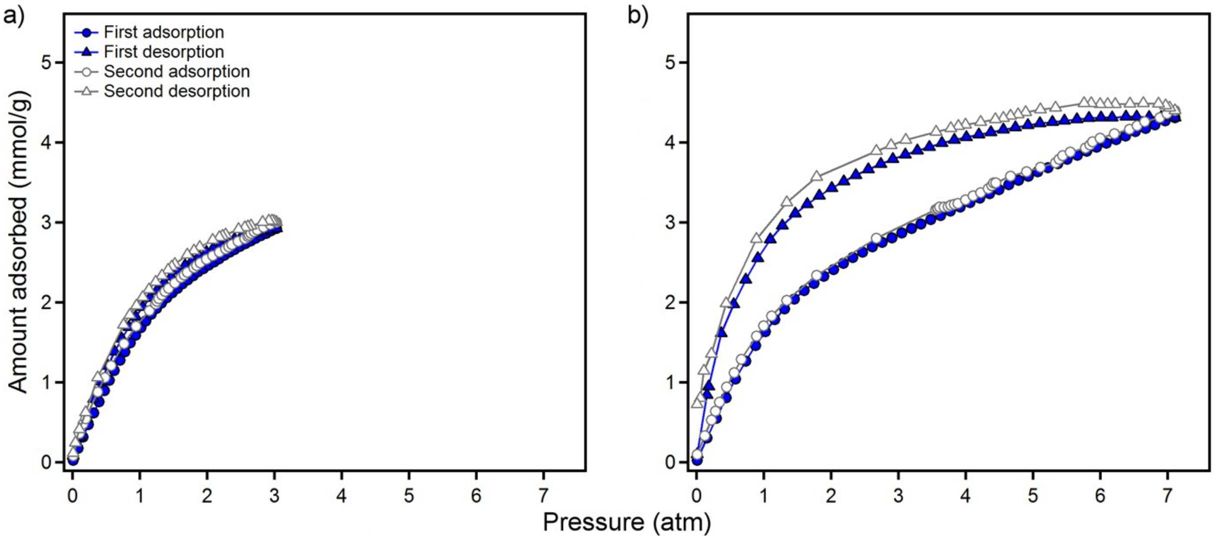

**Fig. S17.** Experimental $CO_2$ adsorption/desorption cycles at 298 K up to 3 atm a) and 7atm b). In both cases: Filled and empty symbols correspond to adsorption and desorption isotherms, respectively. The first and second adsorption/desorption cycles are depicted in dark and light blue, respectively.

To quantify if the differences between adsorption cycles are significant, the ratio between the first and the second cycles was estimated. Equations 1 and 2 indicate how the ratios were calculated:

$$Ratio_{adsorption} = \left(\frac{adsorbed\ amount_{cycle\ 2}}{adsorbed\ amount_{cycle\ 1}}\right)_{at\ the\ same\ pressure\ point} \quad \text{Eq. 1}$$

$$Ratio_{desorption} = \left(\frac{adsorbed\ amount_{cycle\ 2}}{adsorbed\ amount_{cycle\ 1}}\right)_{at\ the\ same\ pressure\ point} \quad \text{Eq. 2}$$

First and second adsorption isotherms were not gathered at the same pressure points. Thus, polynomial fits were performed to quantify the difference between cycles. In the case of adsorption/desorption cycles gathered up to 3.0 atm, polynomials of order 4, 5, 6, and 7 were explored as illustrated in Fig. S18. The residual analysis indicates that the polynomial of order 7 fits the isotherms best. The same analysis for the adsorption/desorption cycles gathered up to 7.0 atm shows that the polynomial of order 9 fits the isotherms best.

In the case where the differences are not significant, the ratio between isotherms should be close to one. However, as the differences increase, the ratio between isotherms deviates from one. Figs. S19 and S21 show the results for the adsorption/desorption cycles up to 3.0 and 7.0 atm, respectively. For instance, in the adsorption/desorption cycles, it is observed that the ratio between the first and the second cycles for the adsorption and desorption isotherms at pressures higher than 1.0 atm are close to one, which means that at high pressures the differences between the cycles are not significant. At pressures lower than 1 atm, the ratio between cycles deviates from one, reaching as high as eight, although this is largely due to the small numbers involved in the calculation. These results indicate that the structural changes are reversible upon adsorption/desorption cycles.

a) polynomial fit: firt adsorption

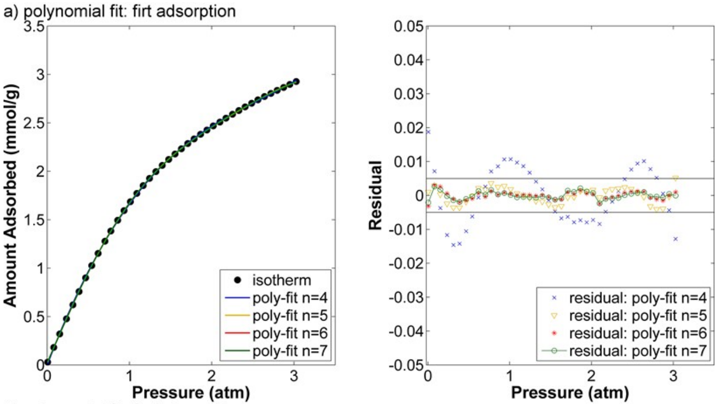

b) polynomial fit: first desorption

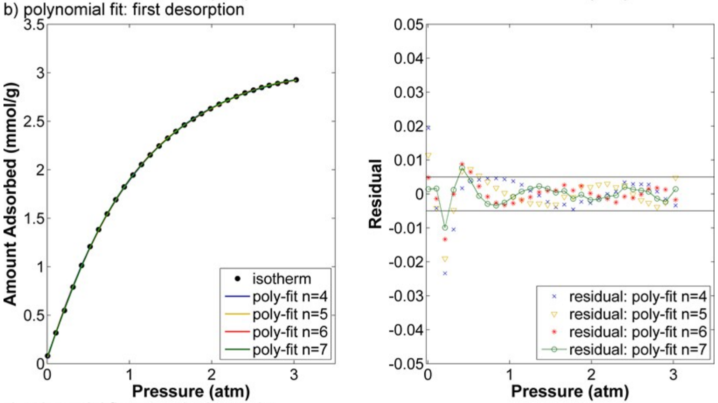

c) polynomial fit: second adsorptoin

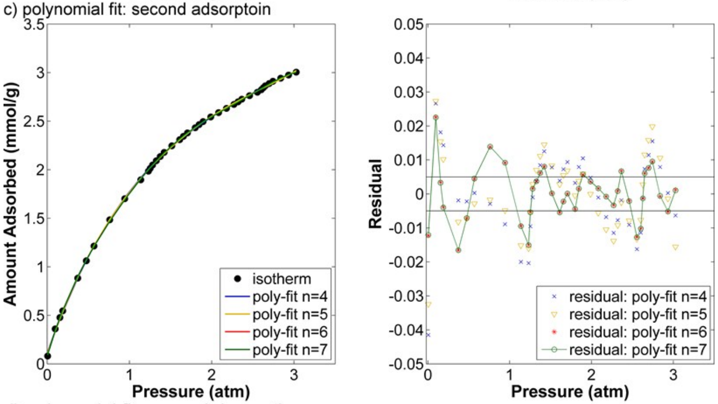

d) polynomial fit: second desorption

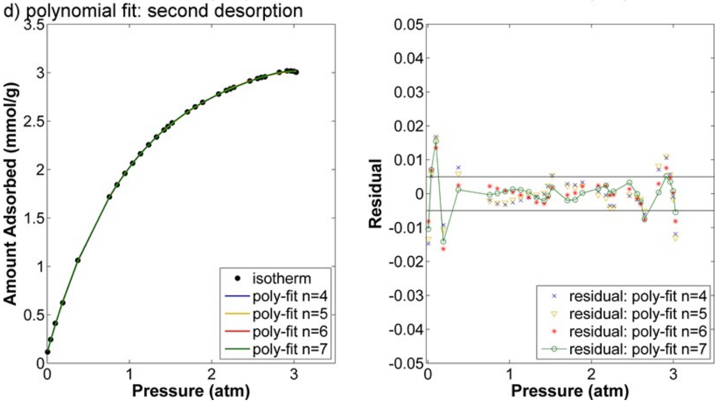

**Figure S18**. Polynomial fit and residuals for adsorption/desorption cycles gathered up to 3.0 atm

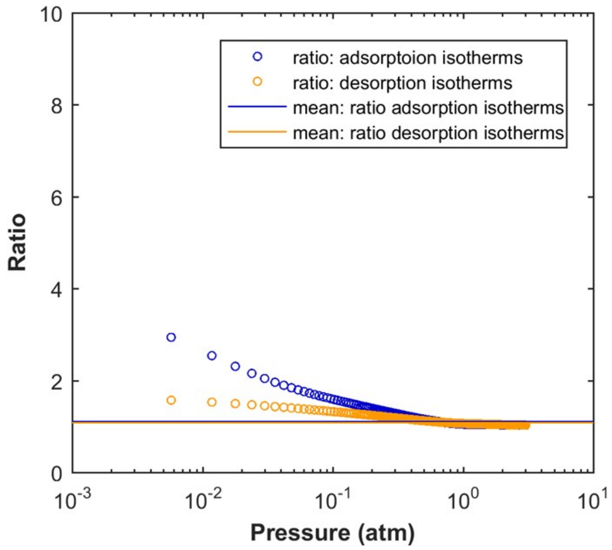

**Fig. S19** Ratio between adsorption isotherm cycles and desorption isotherm cycles for isotherms gathered up to 3.0 atm.

a) polynomial fit: firt adsorption

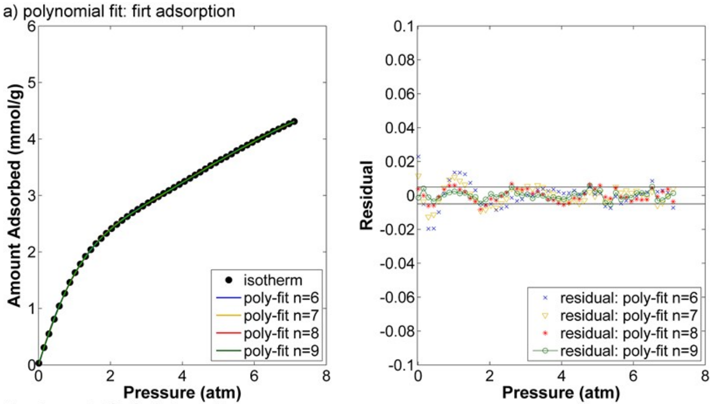

b) polynomial fit: first desorption

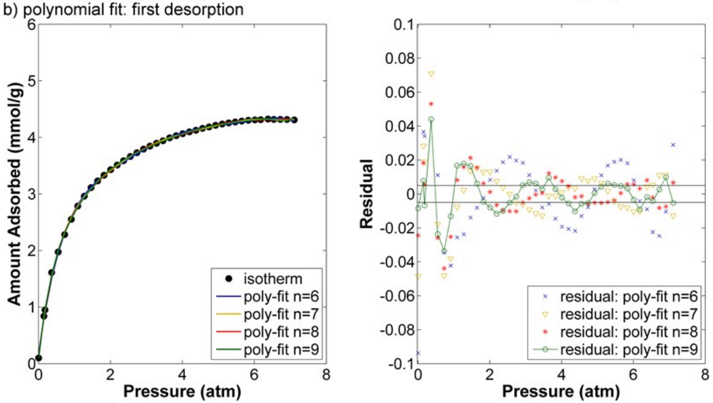

c) polynomial fit: second adsorptoin

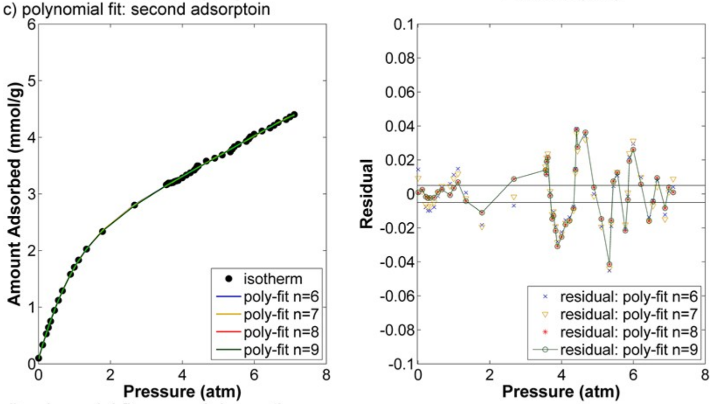

d) polynomial fit: second desorption

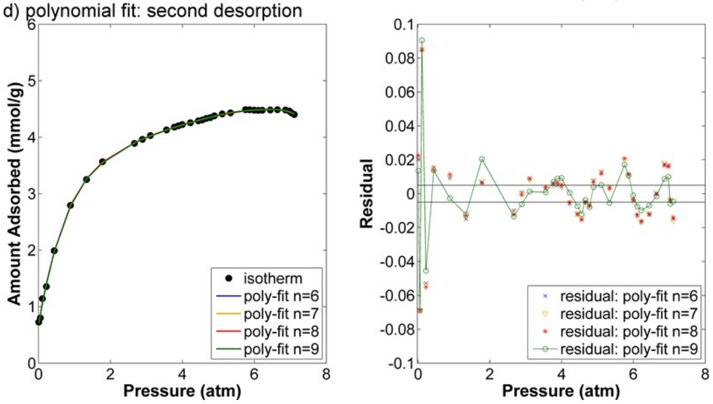

**Fig. S20** Polynomial fit and residuals for adsorption/desorption cycles gathered up to 7.0 atm

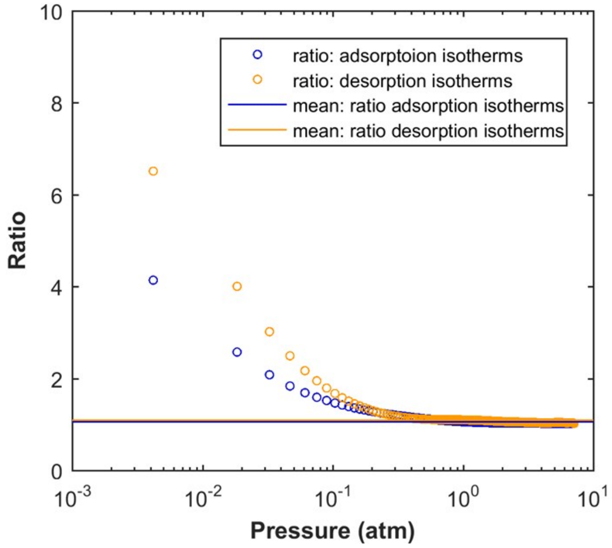

**Fig. S21** Ratio between adsorption isotherm cycles and desorption isotherm cycles for isotherms gathered up to 7.0 atm.

## Section S7. Implications on CPL-4 and CPL-5

**Table S4.** Unit cell parameters for the crystallographic structure of the CPL-4-(***a***) and for the structure including the unit cell deformations (δ= 2.26 % for CPL-4-(***k***)).

| **Unit cell parameter** | CPL-4-(***a***) | CPL-4-(***k***) |
|---|---|---|
| *a* (Å) | 4.7083 | 4.7083 |
| *b* (Å) | 31.011 | 31.712 |
| *c* (Å) | 10.980 | 11.354 |
| *α* (degrees) | 90.000 | 90.000 |
| *β* (degrees) | 96.145 | 95.610 |
| *γ* (degrees) | 90.000 | 90.000 |

**Table S5.** Unit cell parameters for the crystallographic structure of the CPL-5-(***a***) and for the structure including the unit cell deformations (δ= 2.26 % for CPL-5-(***k***)).

| **Unit cell parameter** | CPL-5-(***a***) | CPL-5-(***k***) |
|---|---|---|
| *a* (Å) | 4.7109 | 4.7109 |
| *b* (Å) | 31.858 | 32.578 |
| *c* (Å) | 11.002 | 11.377 |
| *α* (degrees) | 90.000 | 90.000 |
| *β* (degrees) | 96.008 | 95.473 |
| *γ* (degrees) | 90.000 | 90.000 |

**Table S5.** Unit cell parameters for the crystallographic structure of the CPL-4 structure including the unit cell deformations: δ = 3.26, 4.26, and 5.26%.

| **Unit cell parameter** | δ = 3.26% | δ = 4.26% | δ = 5.26% |
|---|---|---|---|
| *a* (Å) | 4.7083 | 4.7083 | 4.7083 |
| *b* (Å) | 32.022 | 32.332 | 32.642 |
| *c* (Å) | 11.354 | 11.354 | 11.354 |
| *α* (degrees) | 90.000 | 90.000 | 90.000 |
| *β* (degrees) | 95.610 | 95.610 | 95.610 |
| *γ* (degrees) | 90.000 | 90.000 | 90.000 |

**Table S6.** Unit cell parameters for the crystallographic structure of the CPL-5 structure including the unit cell deformations: δ = 3.26, 4.26, and 5.26%.

| **Unit cell parameter** | δ = 3.26% | δ = 4.26% | δ = 5.26% |
|---|---|---|---|
| *a* (Å) | 4.7109 | 4.7109 | 4.7109 |
| *b* (Å) | 32.578 | 32.897 | 33.215 |
| *c* (Å) | 11.377 | 11.377 | 11.377 |
| *α* (degrees) | 90.000 | 90.000 | 90.000 |
| *β* (degrees) | 95.473 | 95.473 | 95.473 |
| *γ* (degrees) | 90.000 | 90.000 | 90.000 |

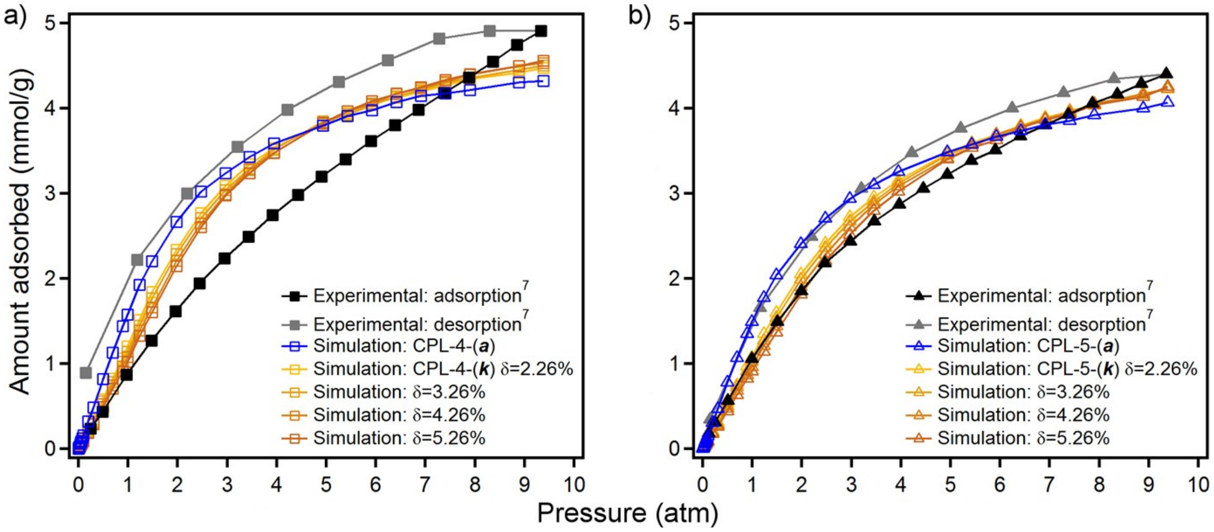

**Fig. S22.** Comparison between the simulated (empty symbols) and experimental[7] (solid symbols) $CO_2$ adsorption/desorption isotherms at 298 K for a) CPL-4 and b) CPL-5. The simulated isotherms were obtained with CPL-4-(***a***) and CPL-5-(***a***) and structures including unit cell deformations as listed in Tables S3 and S4. The observable hysteresis for both materials suggest, similar to CPL-2, the presence of sort of structural changes upon adsorption. Up to 9 atm, the CPL-4 exhibit a higher hysteresis than CPL-5, which could be consequence of higher structure-flexibility upon $CO_2$ adsorption.

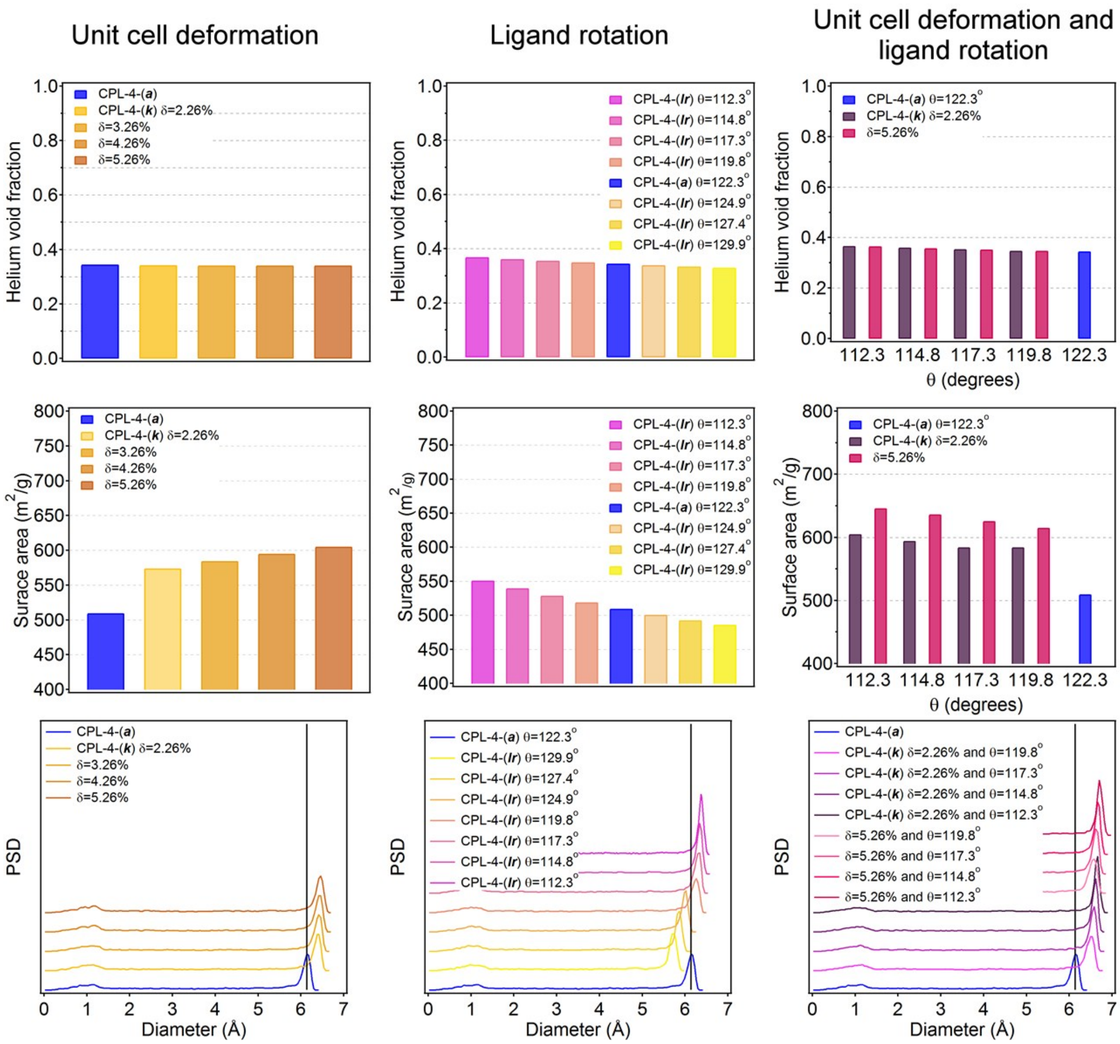

**Fig. S23** Effect of the structural changes on CPL-4 textural properties (helium void fraction, nitrogen-accessible surface area, and pore size distribution). Each column corresponds to a structural change, while each row corresponds to a textural property. The used colors are consistent with the colors for the simulated isotherms in Figs. S22, S25, and S26.

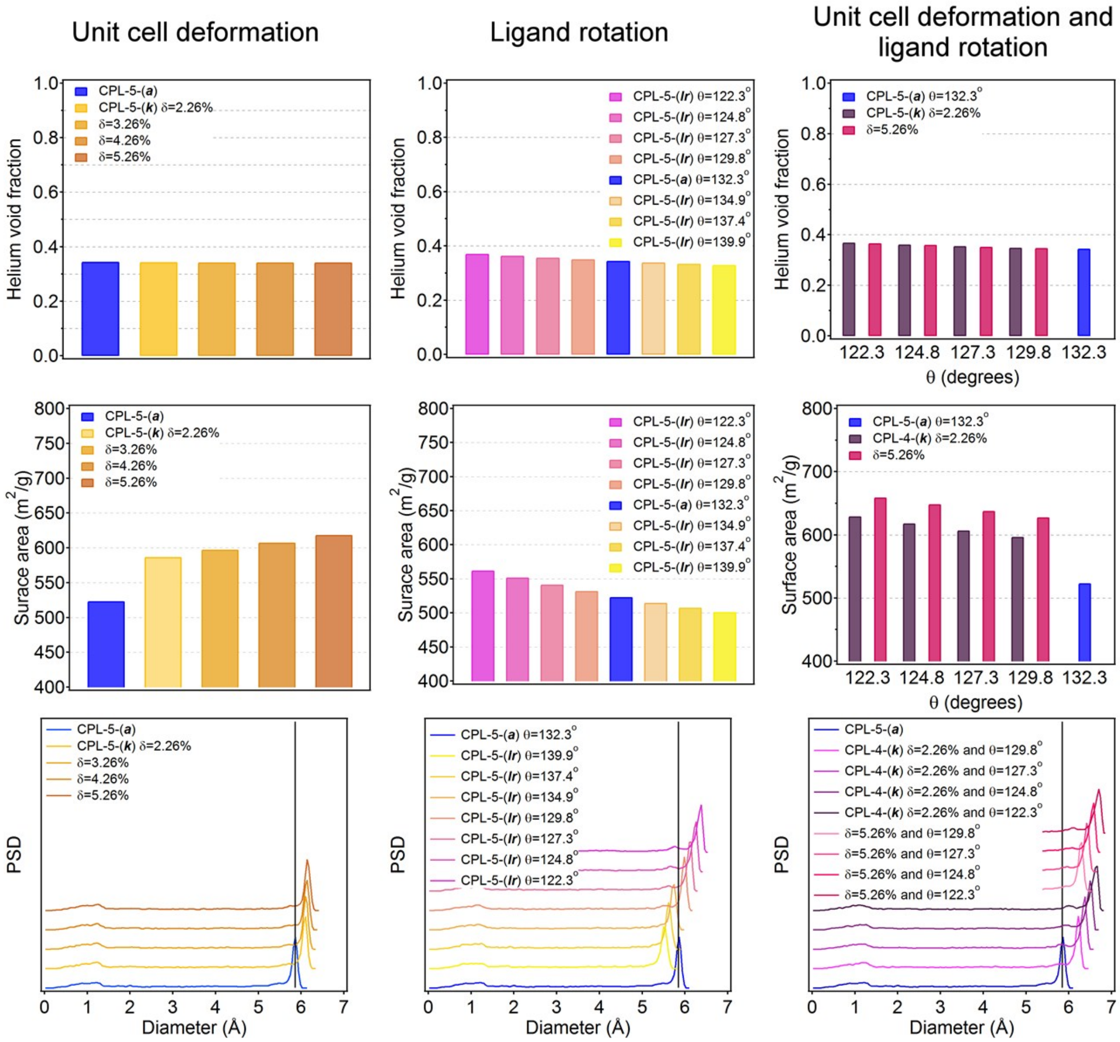

**Figure S24.** Effect of the structural changes on CPL-5 textural properties (helium void fraction, nitrogen-accessible surface area, and pore size distribution). Each column corresponds to a structural change, while each row corresponds to a textural property. The used colors are consistent with the colors for the simulated isotherms in Figs. S22, S25, and S26.

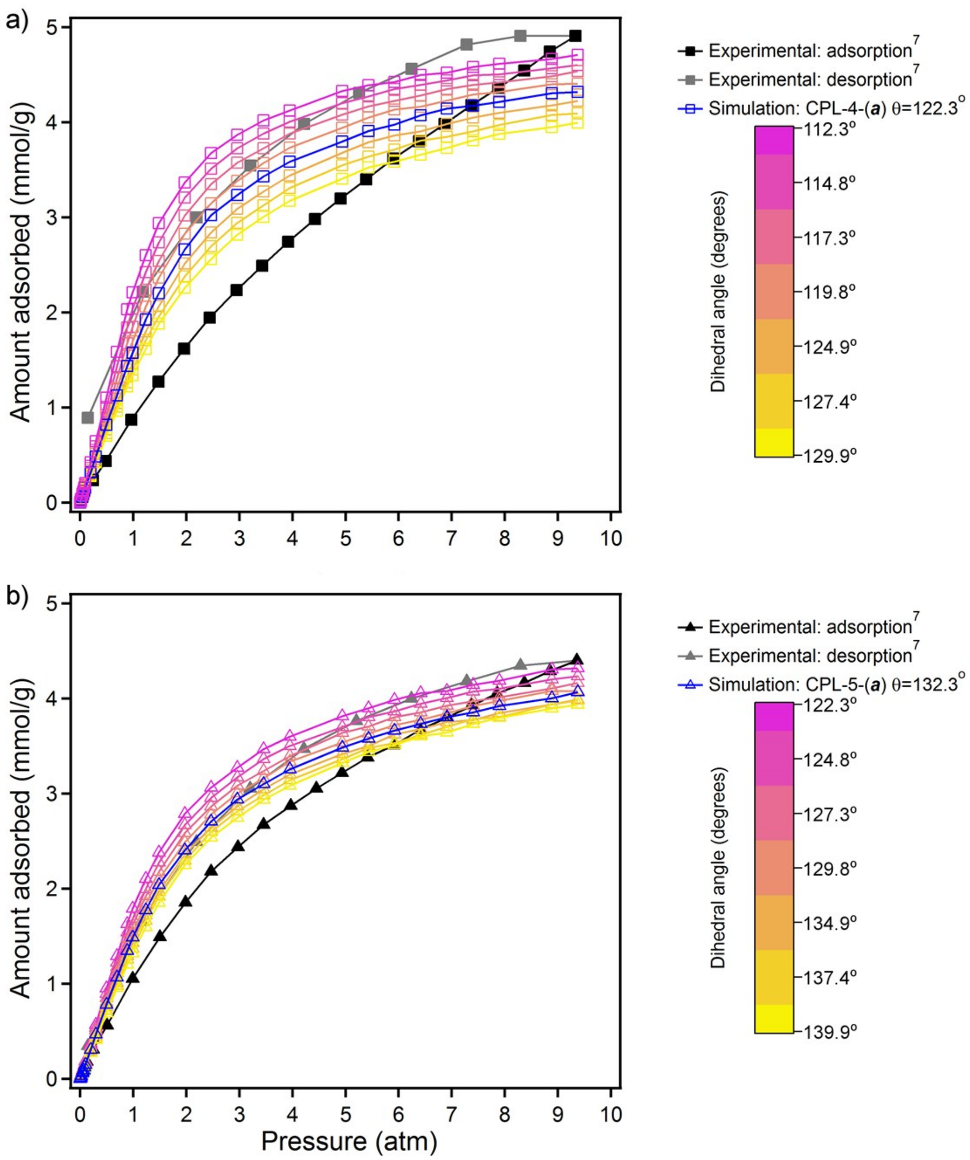

**Figure S25.** Comparison between the simulated (empty symbols) and experimental[7] (solid symbols) $CO_2$ adsorption/desorption isotherms at 298 K for a) CPL-4 and b) CPL-5. The simulated isotherms were obtained for CPL-4-(***lr***) and CPL-5-(***lr***) for different ligand rotations (color gradient) and for CPL-4-(***a***) and CPL-5-(***a***) (blue).

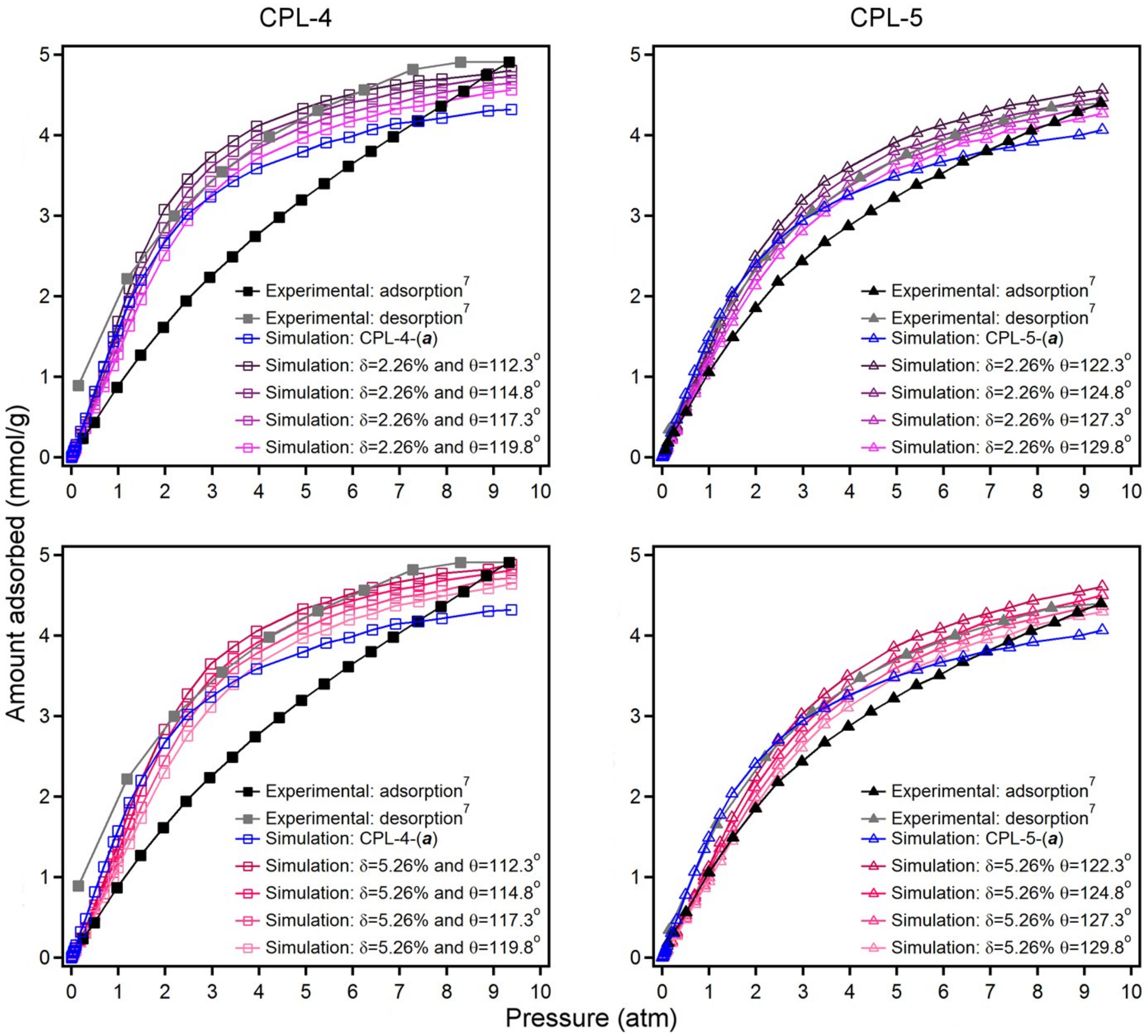

**Figure S26.** Comparison between the simulated and experimental[7] $CO_2$ adsorption and desorption isotherms at 298 K for CPL-4 and CPL-5. The simulated isotherms were obtained by combining unit cell deformations and ligand rotations. The isotherms are also compared with the adsorption isotherm obtained with the CPL-4-(***a***) and CPL-5-(***a***) structures.

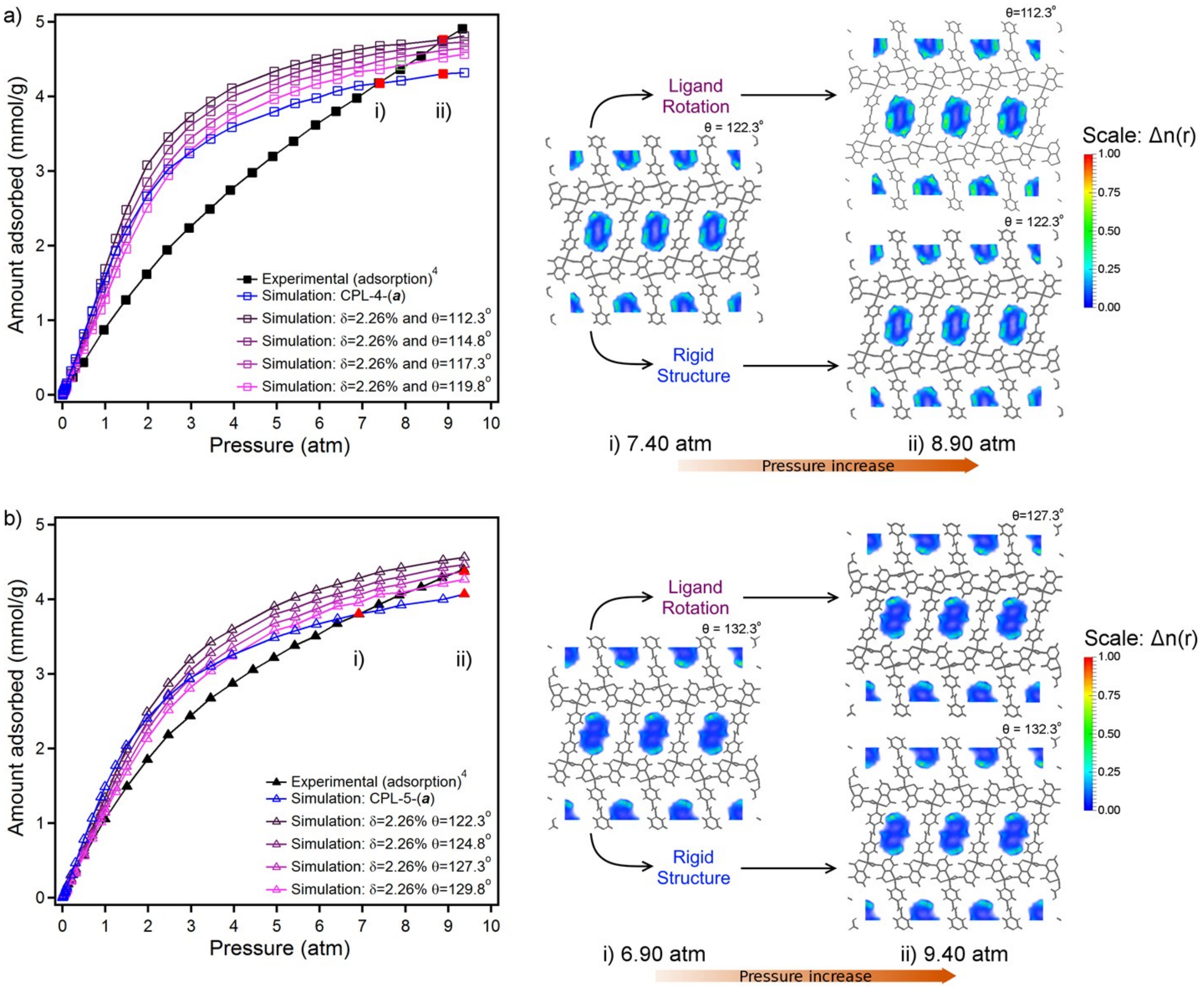

**Figure S27.** $CO_2$ density maps on a) CPL-4 and b) CPL-5 at 298 K and pressures indicated with labels i) and ii) (red markers). The density maps on the rigid structures and considering structures with the *abp* and *bpe* ligands rotation for CPL-4 and CPL-5, respectively.

## REFERENCES

1 R. Matsuda, T. Tsujino, H. Sato, Y. Kubota, K. Morishige, M. Takata and S. Kitagawa, *Chem. Sci.*, 2010, **1**, 315–321.

2 R. Matsuda, R. Kitaura, Y. Kubota, T. C. Kobayashi, M. Takata and S. Kitagawa, *Microporous Mesoporous Mater.*, 2010, **129**, 296–303.

3 K. Riascos-Rodríguez, A. J. Schroeder, M. R. Arend, P. G. Evans and A. J. Hernández-Maldonado, *Dalton Trans.*, 2014, **43**, 10877–10884.

4 O. J. García-Ricard and A. J. Hernández-Maldonado, *J. Phys. Chem. C*, 2010, **114**, 1827–1834.

5 C. E. Wilmer, O. K. Farha, T. Yildirim, I. Eryazici, V. Krungleviciute, A. A. Sarjeant, R. Q. Snurr and J. T. Hupp, *Energy Environ. Sci.*, 2013, **6**, 1158.

6 R. Matsuda, R. Kitaura, S. Kitagawa, Y. Kubota, T. C. Kobayashi, S. Horike and M. Takata, *J. Am. Chem. Soc.*, 2004, **126**, 14063–14070.

7 O. J. García-Ricard, J. C. Silva-Martínez and A. J. Hernández-Maldonado, *Dalt. Trans.*, 2012, **41**, 8922–30.

8 S. Brunauer, P. H. Emmett and E. Teller, *J. Am. Chem. Soc.*, 1938, **60**, 309–319.

9 J. Rouquerol, P. Llewellyn and F. Rouquerol, in *Characterization of Porous Solids VII Proceedings of the 7th International Symposium on the Characterization of Porous Solids (COPS-VII), Aix-en-Provence, France, 26-28 May 2005*, eds. P. L. Llewellyn, F. Rodriquez-Reinoso, J. Rouqerol and N. Seaton, Elsevier, 2007, pp. 49 – 56.